PNAS

Supporting Information for

Direct measurement of dynamic attractant gradients reveals breakdown of the Patlak-Keller-Segel chemotaxis model

Trung V. Phan[1,†], Henry H. Mattingly[2,†], Lam Vo[1], Jonathan S. Marvin[3], Loren L. Looger[3,4], Thierry Emonet[1,5,6,*]

Author affiliations: [1] Department of Molecular, Cellular, and Developmental Biology, Yale University, New Haven, CT; [2] Center for Computational Biology, Flatiron Institute, New York, NY; [3] Janelia Research Campus, Howard Hughes Medical Institute, Ashburn, VA; [4] Howard Hughes Medical Institute, Department of Neurosciences, University of California, San Diego, La Jolla, CA; [5] Quantitative Biology Institute, Yale University, New Haven, CT; and [6] Department of Physics, Yale University, New Haven, CT.

[†] These authors contribute equally to this work
[*] To whom correspondence may be addressed

Thierry Emonet
Email: thierry.emonet@yale.edu

This PDF file includes:

Supporting Information Text

Local drop in oxygen concentration is expected to be proportional to bacterial density.

We model dissolved oxygen concentration O with the following dynamics, averaged over the width of the channel:

$$\partial_t O = D_O\left(\partial_{xx} O + \partial_{yy} O\right) - k_o \frac{O}{O + K_O}\, B(x,y)$$

where x is the direction of the long channel, y is the vertical position in the channel, B is bacterial density, D_O is the diffusivity of oxygen in water, k_O is the maximum consumption rate of oxygen by bacteria, and K_O is the Monod constant of oxygen consumption. Because the channel depth $L = 100\ \mu\text{m}$ is shallow compared to its width (1.2 mm), we can neglect transfer of oxygen into the channel from the side walls.

This PDE is paired with boundary conditions:

$$O(x, y = 0) = O_{out}.$$

$$\left[\partial_y O(x,y)\right]_{y=L} = 0$$

The first boundary condition fixes the oxygen concentration at the water-PDMS interface to O_{out}. The second condition reflects the fact that the glass slide is impermeable to oxygen.

Assuming that K_O is small compared to the minimum oxygen concentration, that variations in cell density B in the y direction are negligible, and that the cells form a quasi-stationary traveling wave with moving reference frame $z = x - c\,t$, we get:

$$-c\,\partial_z O = D_O\left(\partial_{zz} O + \partial_{yy} O\right) - k_o\, B(z).$$

Since the wave is much wider than the depth of the channel, variations in oxygen along the y-direction are much larger than those in the z-direction:

$$\partial_{yy} O - \frac{k_o}{D_O}\, B(z) = 0$$

Integrating once:

$$\partial_y O - \frac{k_o}{D_O}\, B(z)\, y + a_1 = 0$$

Applying the boundary condition at $y = L$:

$$-\frac{k_o}{D_O}\, B(z)\, L + a_1 = 0$$

$$a_1 = \frac{k_o}{D_O}\, B(z)\, L$$

$$\partial_y O - \frac{k_o}{D_O}\, B(z)\,(y - L) = 0$$

Integrating again:

$$O(z,y) - \frac{k_o}{D_O}\, B(z)\left(\frac{y^2}{2} - L\, y\right) + a_2 = 0$$

Applying the boundary condition at $y = 0$:

$$O_{out} + a_2 = 0$$

$$a_2 = -O_{out}.$$

Together:

$$O(z,y) - \frac{k_o}{D_O}\, B(z)\, y\left(\frac{y}{2} - L\right) - O_{out} = 0$$

$$O_{out} - O(z,y) = \frac{k_o}{D_O}\, B(z)\, y\left(L - \frac{y}{2}\right).$$

Averaging the drop in oxygen over the channel depth:

$$\langle \Delta O \rangle_y(z) = \langle O_{out} - O(z,y) \rangle_y = \frac{1}{L}\int_0^L \frac{k_o}{D_O}\, B(z)\, y\left(L - \frac{y}{2}\right) dy$$

$$= \frac{1}{L}\frac{k_o}{D_O} B(z)\left(L\frac{L^2}{2} - \frac{L^3}{6}\right)$$

$$= \frac{L^2}{3}\frac{k_o}{D_O} B(z).$$

Thus, we expect that the local drop in oxygen concentration at position z in the wave scales like the channel depth squared, L^2, and is proportional to the local cell density $B(z)$.

Conversion of fluorescence intensities to aspartate concentration and bacterial density.

The main challenge in performing the calibrations of OD and Asp concentration in each experiment is that the depths of the microfluidic devices vary by about +/-10% across devices, and they also vary with position within one device. But we have enough information to correct for these variations in each experiment.

First, we model GFP and RFP intensity as:

$$GFP(x) = I\big(Asp(x)\big)\, H(x) + DC$$

$$RFP(x) = k_{RFP}\, OD(x)\, H(x) + DC,$$

where DC is the camera dark current intensity, $H(x)$ the is spatially-varying device depth, k_{RFP} is the linear transformation from OD of cells to RFP intensity, and $I(Asp)$ is the sensor emission intensity per unit device depth at an aspartate concentration Asp. We also need a model for the sensor calibration curve. This is the data shown in Fig. 1B:

$$GFP(Asp) = I(Asp)\, H + DC,$$

which depends on the depth of the device used for calibration, H. After shifting and normalizing GFP intensity:

$$\frac{GFP(Asp) - GFP(0\ \mu M)}{GFP(100\ \mu M) - GFP(0\ \mu M)} = \frac{I(Asp) - I(0\ \mu M)}{I(100\ \mu M) - I(0\ \mu M)} \equiv F(Asp).$$

Normalizing this way eliminates differences in height between the experimental devices and the device used for calibration, and it removes the DC intensity.

The first image of each experiment has uniform aspartate at known concentration, 100 uM, with intensity $GFP(100\ \mu M, x) = I(100\ \mu M)\ H(x) + DC$. Also, the last image of each experiment has no aspartate, just sensor, with intensity $GFP(0\ \mu M, x) = I(0\ \mu M)\ H(x) + DC$. We thus compute the aspartate concentration as a function of position and time in each experiment using:

$$Asp(x,t) = F^{-1}\left(\frac{GFP(x,t) - GFP(0\ \mu M, x)}{GFP(100\ \mu M, x) - GFP(0\ \mu M, x)}\right).$$

We can use a similar approach for converting RFP intensity to concentration of bacteria in units of OD. Again, we use the first aspartate image to correct for height variations within the experimental device:

$$OD(x,t) = \frac{RFP(x,t) - DC}{GFP(100\ uM\ Asp, x, t_0) - GFP(0\ \mu M, x, t_N)} \frac{\langle GFP(100\ uM\ Asp) - GFP(0\ uM\ Asp)\rangle}{\langle RFP/OD\rangle},$$

but there is another factor to convert to OD, $\frac{\langle GFP(100\ uM\ Asp)\rangle - DC}{\langle RFP/OD\rangle}$. The numerator of this factor is the GFP intensity of the sensor with 100 μM aspartate, averaged over many devices and positions with the devices:

$$\langle GFP(100\ uM\ Asp) - GFP(0\ uM\ Asp)\rangle = \big(I(100\ \mu M) - I(0\ \mu M)\big)\ \langle H\rangle,$$

where $\langle H\rangle$ is the (unknown) average depth over positions and devices. The denominator $\langle RFP/OD\rangle$ is the RFP intensity per unit OD averaged over devices and positions in devices. Specifically, we measured the RFP intensity of OD6 bacterial suspension in multiple devices:

$$\langle RFP(OD6)\rangle = k_{RFP} * 6 * \langle H\rangle + DC,$$

then subtract the DC intensity and divide by 6 OD:

$$\left\langle \frac{RFP}{OD} \right\rangle = \frac{1}{6}\ (\langle RFP(OD6)\rangle - DC) = k_{RFP}\ \langle H\rangle.$$

Figure S5 shows that RFP intensity is proportional to bacterial density. Using averages over devices ensures that the average height $\langle H\rangle$ cancels out in the numerator and denominator:

$$\frac{\langle GFP(100\ uM\ Asp) - GFP(0\ uM\ Asp)\rangle}{\langle RFP/OD\rangle} = \frac{\big(I(100\ \mu M) - I(0\ \mu M)\big)\ \langle H\rangle}{k_{RFP}\ \langle H\rangle} = \frac{I(100\ \mu M) - I(0\ \mu M)}{k_{RFP}}.$$

Thus,

$$\frac{RFP(x,t) - DC}{GFP(100\ uM\ Asp, x, t_0) - GFP(0\ \mu M, x, t_N)} \frac{\langle GFP(100\ uM\ Asp) - GFP(0\ uM\ Asp)\rangle}{\langle RFP/OD\rangle}$$

$$= \frac{k_{RFP}\ OD(x,t)\ H(x)}{\big(I(100\ \mu M) - I(0\ \mu M)\big)\ H(x)} \frac{I(100\ \mu M) - I(0\ \mu M)}{k_{RFP}}$$

$$= OD(x,t).$$

Error analysis and fitting.

To quantify the goodness of fit between the left-hand side (LHS) and right-hand side (RHS) of each equation, we compute the mean squared error (MSE) between them. The MSE is defined as:

$$MSE = \frac{1}{N_z}\sum_i \frac{\big(LHS(z_i) - RHS(z_i)\big)^2}{\sigma^2(z_i)},$$

where z_i is the ith position at which the LHS and RHS were measured; N_z is the total number positions; $LHS(z_i)$ and $RHS(z_i)$ are the averages over replicates of the LHS and RHS of each equation; and the uncertainty of each point is

$$\sigma^2(z_i) = \sigma^2_{LHS}(z_i) + \sigma^2_{RHS}(z_i).$$

To get the uncertainties, we need to clarify that terms with derivatives were computed by fitting splines to each replicate and then computing the derivative of the spline. Since the spline fits are estimates of the *mean* of their corresponding terms, we can get the uncertainty of the mean by computing the *standard deviation* of the spline over replicates at each point. For terms that did not use splines, we compute the *standard error* over the replicates at each point.

Eqn. 3 has derivatives only on the LHS. Denote the spline fit of A in experiment j as $A_j(z)$, and the average of the splines as $\langle A_j \rangle$. The uncertainty of the LHS, $-c\,\partial_z A - D_A \partial_z^2 A$, is then

$$\sigma^2_{LHS}(z_i) = \left(\langle c\rangle^2 + \frac{Var(c)}{N_{reps}-1}\right)\left(\big(\partial_z\langle A_j\rangle(z_i)\big)^2 + Var\big(\partial_z A_j\big)(z_i)\right) - \langle c\rangle^2\left(\partial_z\langle A_j\rangle(z_i)\right)^2 + D_a^2\, Var\big(\partial_z^2 A_j\big)(z_i),$$

using $Var(X\,Y) = \big(\langle X\rangle^2 + Var(X)\big)\big(\langle Y\rangle^2 + Var(Y)\big) - \langle X\rangle^2\langle Y\rangle^2$. In the first two terms, we propagated uncorrelated errors in c and $\partial_z\langle A\rangle$ to errors in their product. $\langle c\rangle$ is the average speed over replicates for the given condition. Note that $Var(c)$ is divided by $N_{reps} - 1$ to get a standard error, but the variance of the spline terms are not divided by $N_{reps} - 1$, since they are already "averages".

Then, for the KS model of Eqn. 3,

$$\sigma^2_{RHS}(z_i) = \gamma^2\,\frac{1}{N_{reps}-1} Var\left(\frac{A}{A+A_h}B\right)(z_i),$$

while for the modified KS model,

$$\sigma^2_{RHS}(z_i) = \gamma_0^2\,\frac{1}{N_{reps}-1} Var\left(\frac{A}{A+A_h}\frac{B}{B+B_c}\,B\right)(z_i),$$

where $Var(\ \ )$ above is the variance over replicate experiments at a *given* value of the parameters, as would be the case when computing a likelihood function. Dividing by $N_{reps} - 1$ gives the (squared) standard error of the mean over replicates.

The uncertainty of the LHS of Eqn. 4 is:

$$\sigma^2_{LHS}(z_i) = \left(\langle c\rangle^2 + \frac{Var(c)}{N_{reps}-1}\right)\left(\big(\partial_z\langle B\rangle(z_i)\big)^2 + Var\big(\partial_z B_j\big)(z_i)\right) - \langle c\rangle^2\big(\partial_z\langle B\rangle(z_i)\big)^2,$$

where $B_j(z)$ is the spline fit to bacterial density in experiment j.

The error for the RHS of the KS model of Eqn 4. is:

$$\sigma_{RHS}^2(z_i) = D_B^2\, Var\left(\partial_z^2 B_j\right)(z_i) + \chi^2\, Var\left(\partial_z\left(B_j(z_i)\,\partial_z\Phi_j(z_i)\right)\right),$$

where $\Phi_j(z)$ is the spline fit to the perceived signal in experiment j.

The error for the RHS of the modified KS model is:

$$\sigma_{RHS}^2(z_i) = D_B^2\, Var\left(\partial_z^2 B_j\right)(z_i) + \chi_0^2\, Var\left(\frac{1}{1+B(z_i)/B_h}\partial_z\left(B_j(z_i)\,\partial_z\Phi_j(z_i)\right)\right).$$

We neglect the uncertainty in α because that term is negligibly small (see Fig. S4).

Note that when we compute error bars for the LHS and RHS of Eqn. 5, the evolution of bacterial density, we do not include the uncertainty of the conversion from RFP intensity to OD. We exclude this because those errors are 100% correlated on both sides of the equation, so including them would overestimate our uncertainties. After inferring the parameters, we then account for uncertainties in the conversion from RFP to OD in all parameters that have units of OD.

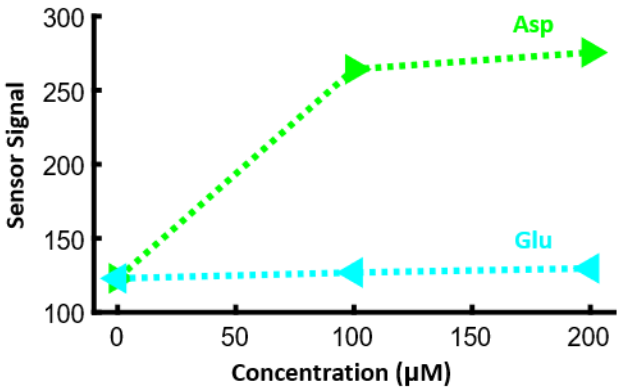

Fig. S1. jAspSnFR3 is specific for aspartate and insensitive to glutamate. Sensor fluorescence emission response to glutamate (Glu, cyan) is negligible compared to the response to aspartate (Asp, green). Concentration values are 0, 100 and $200\ \mu M$ for both amino acids. Data points are averages over an entire sweep of images along the microfluidic device. The same device was used for all Asp concentrations.

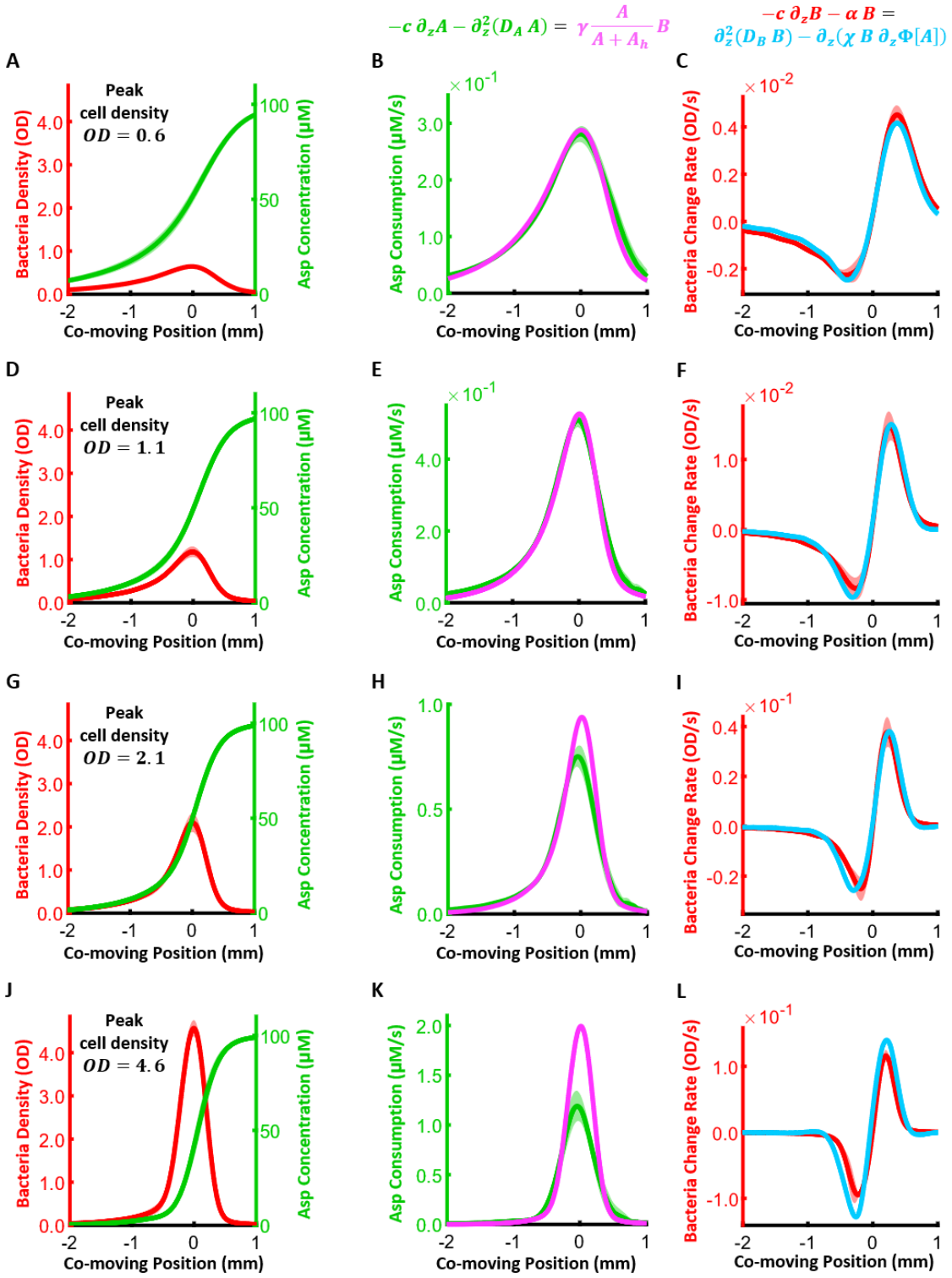

Fig. S2. The standard model for chemotaxis, the Patlak-Keller-Segel (PKS) model, describes the bacterial wave at low cell densities but breaks down at high densities. **(A)** The quasi-steady state profiles in the co-moving frame, of bacteria density (red) and attractant Asp concentration (green), during low cell density migration (OD = 0.6). **(B)** Fitting the Asp dynamics of the PKS model to experimental data (above). $\boldsymbol{A}$ and $\boldsymbol{B}$ are the Asp concentration and the bacteria

density respectively, $\boldsymbol{c}$ is the wave speed, $\boldsymbol{D_A}$ is the molecular diffusion of Asp, $\boldsymbol{\gamma}$ is the maximum consumption rate, $\boldsymbol{A_h}$ is the half-max of the consumption rate, and $\boldsymbol{z = x - c\,t}$ is the coordinate in the co-moving frame ($\boldsymbol{z = 0}$ is set to the peak bacteria density). Green: LHS of the Asp dynamics equation with $\boldsymbol{A}$ and $\boldsymbol{c = 4.4 \pm 0.1\ \mu m/s}$ measured and $\boldsymbol{D_A = 800\ \mu m^2/s}$ (1–5). Magenta: RHS of the Asp dynamics equation with $\boldsymbol{B}$ measured, and $\boldsymbol{\gamma = 0.51 \pm 0.05\ \mu M/OD/s}$ and $\boldsymbol{A_h = 7.6 \pm 3.7\ \mu M}$ fit to match the LHS using the data in **(B). (C)** Fitting the bacterial dynamics of the PKS model to experimental data (above). $\boldsymbol{\Phi[A] = \ln\left(\frac{1+A/K_i}{1+A/K_a}\right)}$ is the cells' perceived signal ($\boldsymbol{K_a \gg A}$ and $\boldsymbol{K_i = 1\ \mu M}$ (6–9)), $\boldsymbol{D_B}$ is the effective bacterial diffusivity, $\boldsymbol{\chi}$ is the chemotactic coefficient, and $\boldsymbol{\alpha = 0.4/hr}$ is the measured growth rate (Methods). Red: LHS of the bacteria dynamics equation with $\boldsymbol{\alpha}$, $\boldsymbol{c}$, and $\boldsymbol{B}$ measured. Cyan: RHS of the bacteria dynamics equation with $\boldsymbol{D_B = 400 \pm 100\ \mu m^2/s}$ and $\boldsymbol{\chi = 3300 \pm 230\ \mu m^2/s}$ fit to match the LHS using the data in **(C). (D,E,F), (G,H,I), (J,K,L)** are the same as **(A,B,C)**, using the same parameters, but for high cell density waves. Wave speeds are $\boldsymbol{c = 5.5 \pm 0.1\ \mu m/s}$ (OD = 1.1), $\boldsymbol{c = 6.4 \pm 0.2\ \mu m/s}$ (OD = 2.1) and $\boldsymbol{c = 7.7 \pm 0.2\ \mu m/s}$ (OD = 4.6). **(E,F), (H,I), (K,L)** magenta and cyan lines are prediction using the same parameter values for $\boldsymbol{\gamma}$, $\boldsymbol{A_h}$, $\boldsymbol{D_B}$, $\boldsymbol{\chi}$ as in **(B,C)**. The shading represents the standard deviation across replicates. Replicate $\boldsymbol{N = 6}$ for **(A,B,C)**, $\boldsymbol{N = 9}$ for **(D,E,F)**, $\boldsymbol{N = 5}$ for **(G,H,I)**, and $\boldsymbol{N = 4}$ for **(J,K,L)**. Uncertainties for the RHS of each equation are not shown for clarity, but were included in the calculation of the mean squared error (SI).

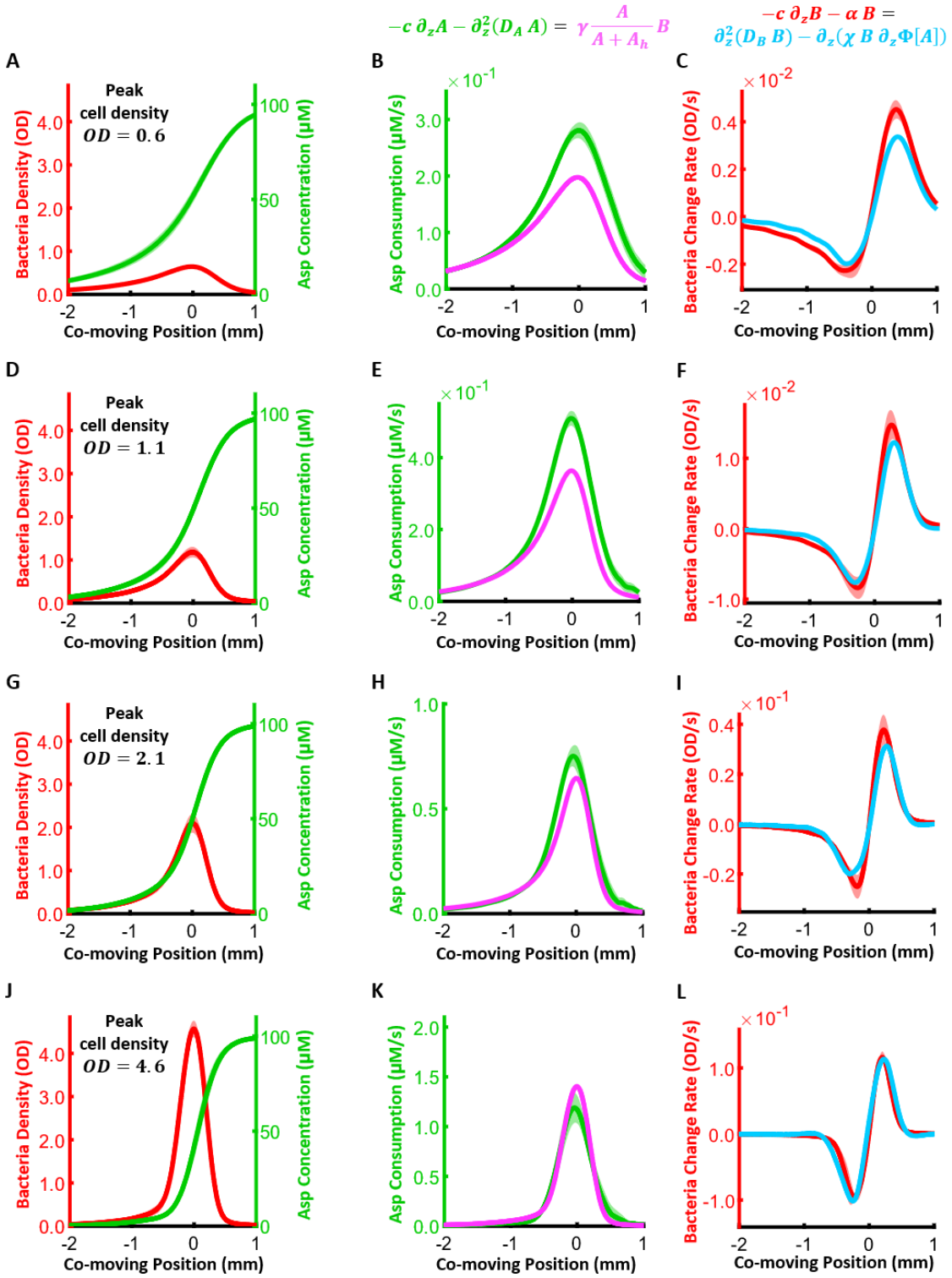

Fig. S3. Conversely, the Patlak-Keller-Segel (PKS) model can be fit to the bacterial wave data at high cell densities, but then fails at low densities. The let column is the same as that of Fig. S2. The green curves in the middle column and the red curves of the right column are also the same as those in Fig. S2. **(B)** Magenta: RHS of the Asp dynamics equation with B measured, and $\gamma = 0.31 \pm 0.03\ \mu M/OD/s$ and $A_h = 0.1 \pm 2.3\ \mu M$ fit to match the LHS using the data in panel **(K).**

(C) Fitting the bacterial dynamics of the PKS model to experimental data (above). Cyan: RHS of the bacteria dynamics equation with $D_B = 360 \pm 160\ \mu m^2/s$ and $\chi = 2800 \pm 320\ \mu m^2/s$ fit to match the LHS using the data in panel **(L)**. **(D,E,F), (G,H,I), (J,K,L)** are the same as **(A,B,C)**, using the same parameters, but for high cell density waves. Wave speeds are $c = 5.5 \pm 0.1\ \mu m/s$ (OD = 1.1), $c = 6.4 \pm 0.2\ \mu m/s$ (OD = 2.1) and $c = 7.7 \pm 0.2\ \mu m/s$ (OD = 4.6). **(E,F), (H,I), (K,L)** magenta and cyan lines are prediction using the same parameter values for γ, A_h, D_B, χ as in **(B,C)**. The shading represents the standard deviation across replicates. Replicate $N = 6$ for **(A,B,C)**, $N = 9$ for **(D,E,F)**, $N = 5$ for **(G,H,I)**, and $N = 4$ for **(J,K,L)**. Uncertainties for the RHS of each equation are not shown for clarity, but were included in the calculation of the mean squared error (SI).

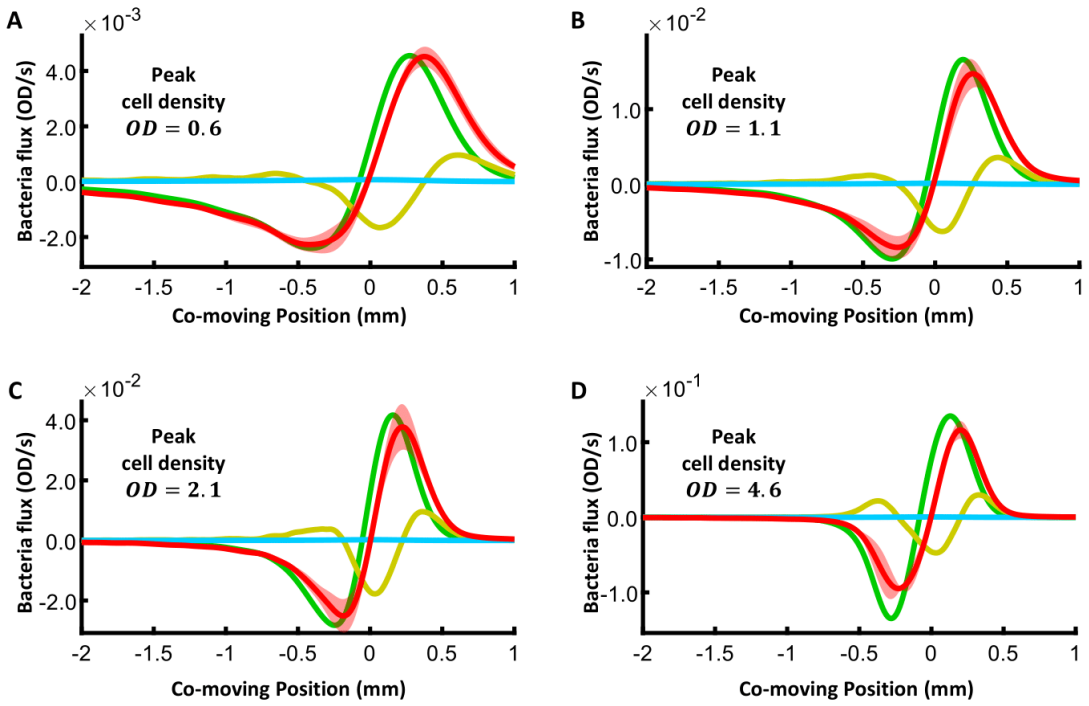

Figure S4. Contribution from growth is negligible compared to the total bacteria flux. We use the best-fit values for the parameters in the extended Patlak-Keller-Segel model to compare different components of the bacterial flux. Green: Chemotactic flux $-\partial_z(\chi[B]B\partial_z\Phi[A])$. Yellow: Diffusion flux $D_B\,\partial_z^2 B$. Cyan: Growth $\alpha\,B$. Red: The measured total bacteria flux $-c\partial_z B$, which is approximately the sum of these three terms. The shading represents the standard deviation across replicates. These are shown for waves with peak bacterial cell density of $\mathrm{OD} = 0.6$ **(A)**, 1.1 **(B)**, 2.1 **(C)**, and 4.6 **(D)**.

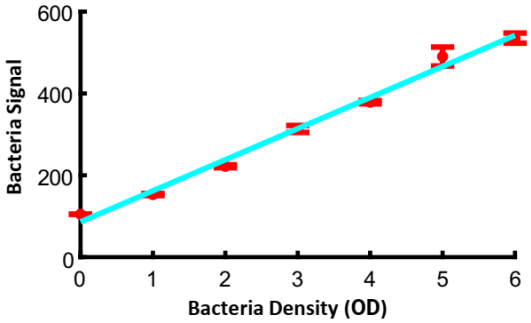

Fig. S5. The bacteria signal (RFP) depends linearly on the bacteria density. Red: RFP fluorescence of uniform cell suspensions of known cell density measured in microfluidic devices using the same procedure as the wave experiment. Cyan: linear fit. The slope has value 76 ± 4 signal-unit/OD, and the goodness-of-fit is $R^2 = 0.99$. Data points are averages over 3 fixed positions on the microfluidic device. The same device was used for all bacteria densities. Note that this data was not used for any calibration—its purpose is to demonstrate that fluorescence depends linearly on bacterial density.

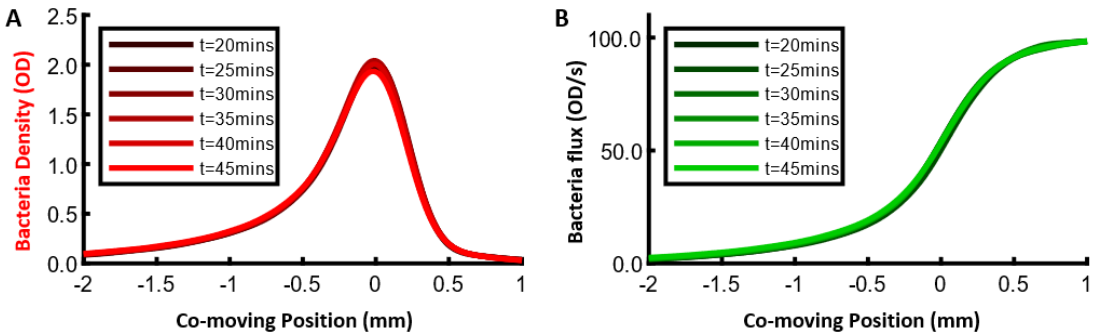

Fig. S6. Time progression of the bacteria density and the aspartate concentration in the co-moving frame. Here we show, using data from one experiment of a travelling wave with peak bacteria cell density of $\mathrm{OD} = 2.1$, that within the co-moving reference frame, the bacteria density and Asp concentration do not change during the last 6 frames, the time range in which analyses were performed. **(A)** Bacterial density. **(B)** Asp concentration.

SI References

1. Fu X, Kato S, Long J, Mattingly HH, He C, Vural DC, et al. Spatial self-organization resolves conflicts between individuality and collective migration. Nature Communications. 2018 Jun 5;9(1):2177.

2. Cremer J, Honda T, Tang Y, Wong-Ng J, Vergassola M, Hwa T. Chemotaxis as a navigation strategy to boost range expansion. Nature. 2019 Nov;575(7784):658–63.

3. Hazel JR, Sidell BD. A method for the determination of diffusion coefficients for small molecules in aqueous solution. Analytical Biochemistry. 1987 Nov 1;166(2):335–41.

4. Ribeiro ACF, Barros MCF, Verissimo LMP, Lobo VMM, Valente AJM. Binary Diffusion Coefficients for Aqueous Solutions of l-Aspartic Acid and Its Respective Monosodium Salt. J Solution Chem. 2014 Feb 1;43(1):83–92.

5. Cremer J, Segota I, Yang C yu, Arnoldini M, Sauls JT, Zhang Z, et al. Effect of flow and peristaltic mixing on bacterial growth in a gut-like channel. PNAS. 2016 Oct 11;113(41):11414–9.

6. Neumann S, Hansen CH, Wingreen NS, Sourjik V. Differences in signalling by directly and indirectly binding ligands in bacterial chemotaxis. The EMBO Journal. 2010 Oct 20;29(20):3484–95.

7. Yang Y, M. Pollard A, Höfler C, Poschet G, Wirtz M, Hell R, et al. Relation between chemotaxis and consumption of amino acids in bacteria. Molecular Microbiology. 2015;96(6):1272–82.

8. Moore JP, Kamino K, Kottou R, Shimizu T, Emonet T. Sensory diversity and precise adaptation enable independent bet-hedging strategies for multiple signals at the same time [Internet]. bioRxiv; 2023 [cited 2023 Feb 16]. p. 2023.02.08.527720. Available from: https://www.biorxiv.org/content/10.1101/2023.02.08.527720v1

9. Mello BA, Tu Y. An allosteric model for heterogeneous receptor complexes: Understanding bacterial chemotaxis responses to multiple stimuli. PNAS. 2005 Nov 29;102(48):17354–9.